

JGR Solid Earth

RESEARCH ARTICLE

10.1029/2020JB019636

Key Point:

- Local GNSS is a useful tool in near-field tsunami hazard analysis

Supporting Information:

- Supporting Information S1

Correspondence to:

A. L. Williamson,
awillia5@uoregon.edu

Citation:

Williamson, A. L., Melgar, D., Crowell, B. W., Arcas, D., Melbourne, T. I., Wei, Y., & Kwong, K. (2020). Toward near-field tsunami forecasting along the Cascadia subduction zone using rapid GNSS source models. *Journal of Geophysical Research: Solid Earth*, 125, e2020JB019636. <https://doi.org/10.1029/2020JB019636>

Received 21 FEB 2020

Accepted 4 AUG 2020

Accepted article online 6 AUG 2020

Toward Near-Field Tsunami Forecasting Along the Cascadia Subduction Zone Using Rapid GNSS Source Models

Amy L. Williamson¹ , Diego Melgar¹ , Brendan W. Crowell² , Diego Arcas³, Timothy I. Melbourne⁴ , Yong Wei^{2,3} , and Kevin Kwong² 

¹Department of Earth Sciences, University of Oregon, Eugene, OR, USA, ²Department of Earth and Space Sciences, University of Washington, Seattle, WA, USA, ³NOAA/Pacific Marine Environmental Lab, Seattle, WA, USA, ⁴Department of Geological Sciences, Central Washington University, Ellensburg, WA, USA

Abstract Over the past 15 years and through multiple large and devastating earthquakes, tsunami warning systems have grown considerably in their efficacy in providing timely and accurate forecasts to affected communities. However, one part of tsunami warning that still needs improvement is forecasts catered to local, near-field communities in the time after an earthquake rupture but before coastal inundation. In this study, we test a rapid, Global Navigation Satellite Systems (GNSS)-driven earthquake characterization model using a large data set of synthetic megathrust ruptures for its near-field tsunami forecasting potential. We also provide a framework for tsunami forecasting that focuses on the likelihood of exceedance of user-defined coastal amplitudes that may be of use in the first 15 min following an earthquake. Specifically, we can estimate the earthquake magnitude, without saturation, for 82% of tested ruptures. We can also identify test ruptures as dominantly thrust events, without analyst guidance for 92% of tested thrust ruptures. Finally, modeling the tsunami component of our rapidly estimated fault rupture leads to greater than 80% accuracy in identifying tsunami impact at key coastal amplitude thresholds. This is promising for near-field warning when the time prior to inundation is limited to tens of minutes. We focus this study on large megathrust ruptures along the quiescent Cascadia subduction zone where there is already a dense GNSS network.

1. Introduction

Following a submarine earthquake, the places that bear the greatest tsunami hazards are local coastal communities. Not only are tsunami amplitudes the highest in the near-field environment but also damaging waves can arrive soon after the earthquake rupture. During the 2011 Tohoku-oki earthquake the first arrival of the tsunami along coastlines in the Miyagi prefecture was 25 min after the rupture began; the tsunami arrived at Sendai almost 70 min after the earthquake (Muhari et al., 2012; Tsuji et al., 2011). More abbreviated, the 2015 Illapel earthquake produced a tsunami that was detected at the nearest coastal tide gauges within 15 min of rupture (Aránguiz et al., 2017; Satake & Heidarzadeh, 2017) while eyewitness reports from the 2010 Maule earthquake identify a coastal arrival within 12 min (Vargas et al., 2011). When the near-field is the target, these abbreviated timeframes challenge the utility of many traditional methods of determining and issuing tsunami warnings. Historically, tsunami hazard assessment and warnings have focused on providing warning from distant tsunami sources using seismic and seafloor data sets (Bernard & Titov, 2015). Tsunami waveforms recorded at open-ocean pressure sensors such as Deep-Ocean Assessment and Reporting of Tsunami (DART) gauges are analyzed in real time to determine appropriate tsunami warnings (Mungov et al., 2013; Percival et al., 2011; Tang et al., 2016). However, submarine instruments, while pivotal for middle and far-field warnings, are in all but a few environments ill positioned for local tsunami warning (Williamson & Newman, 2018). Therefore, seismic data, like W phase, which records information much sooner, is used to quickly assess the potential tsunami hazard for the near field (Kanamori & Rivera, 2008). While useful for warnings, seismic data takes time to converge on a stable and accurate magnitude for very large events. Even with a timely and correct magnitude, the expected tsunami hazard is still uncertain as little else is known about the earthquake rupture.

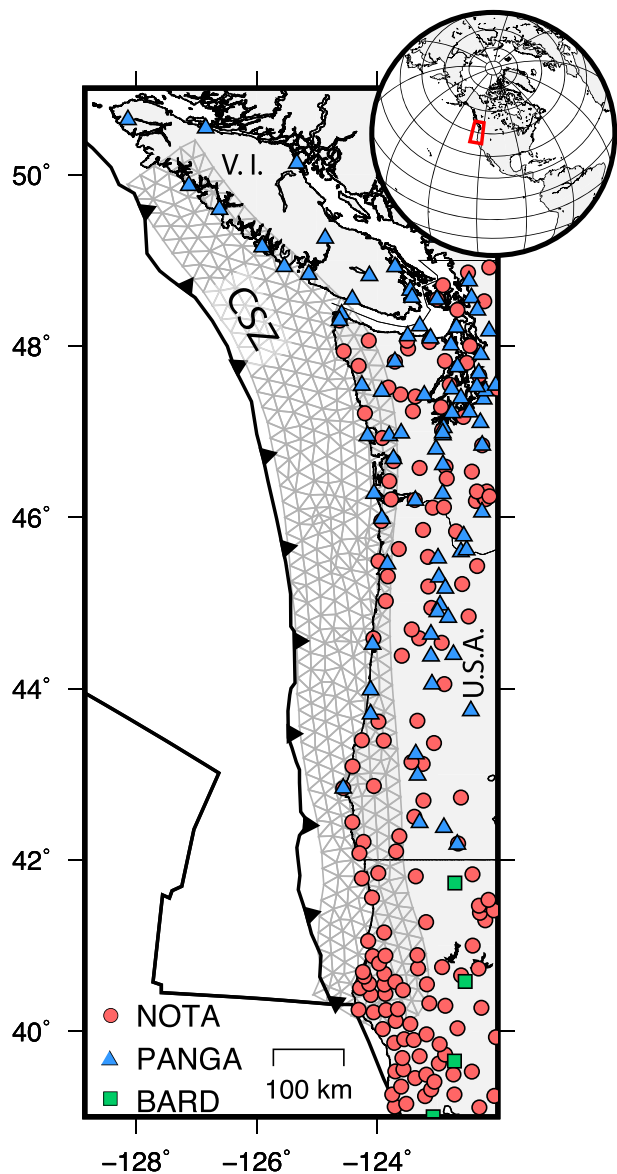


Figure 1. View of the Cascadia subduction zone and all regional 1 Hz GNSS stations with potential real-time capabilities. Gray meshed area shows the map view of the subduction fault geometry and subfault size for scenario ruptures. Plate boundaries are drawn as defined by Bird (2003). The Cascadia subduction zone is abbreviated at CSZ. Vancouver Island is marked as V.I.

source products derived from high-rate and real time GNSS data for potential earthquakes originating on the Cascadia margin. Specifically, we focus on two aspects. First, we analyze the ability of regional GNSS sensors to rapidly estimate characteristics of an offshore earthquake such as magnitude, focal mechanism, and fault slip. Second, we show how well automated GNSS-driven slip models can reproduce observed tsunami amplitudes at local coastlines, proposing an assessment method based on user defined thresholds that we believe is beneficial for local tsunami warning. Our primary concern is providing accurate and timely information on expected tsunami amplitudes minutes after earthquake rupture. While GNSS source products have been used in the past to determine characteristics of the earthquake rupture, this study goes one step further and looks at how these products translate to local tsunami intensity forecasting abilities. Successful tsunami hazard assessment using GNSS data, while not a replacement for direct tsunami observations, could fill in the data gap between tsunami generation and coastal inundation in the near field.

In complement to seismic data sets, displacements retrieved and processed from high-rate (1 Hz) real-time Global Navigation Satellite Systems (GNSS) sensors may provide useful information during earthquake rupture and can be leveraged to provide local tsunami warnings within the minutes after origin time. Unlike seismic data, near-field GNSS displacement data does not saturate due to large motions (Bock et al., 2011). GNSS data can be tested to determine preliminary magnitudes, fault orientations, and slip distributions both for detailed earthquake source studies (e.g., Fang et al., 2014; Gusman et al., 2015; Vigny et al., 2005, 2011; Wright et al., 2012; Yue & Lay, 2011) as well as in real or simulated real-time (e.g., Crowell et al., 2012, 2016; Melgar et al., 2015; Ruhl et al., 2017). Because of this utility, GNSS-focused algorithms have been developed within the earthquake early warning and rapid response community. This includes BEFORES (Bayesian Evidence Based Fault-Orientation and Real-time Earthquake Slip; Minson et al., 2014), G-larms (Geodetic Alarm System; Grapenthin et al., 2014), REGARD (GEONET real-time analysis system; Kawamoto et al., 2016), and GFAST (Geodetic First Approximation of Size and Time; Crowell et al., 2016) among others. Similarly, it has been shown that GNSS waveforms can greatly speed up the calculation of W phase moment tensors which traditionally cannot be computed in the near-field with seismic data alone (Riquelme et al., 2016).

Past studies have also looked at the role of geodetic data in tsunami early warning. A GPS derived earthquake magnitude was determined retroactively for the 2004 Sumatra earthquake by Blewitt et al. (2006), signaling its utility for tsunami warning systems. Sobolev et al. (2007) advocates that using both vertical and horizontal components of GPS within 100 km of the earthquake source can help better resolve slip, leading to better tsunami forecasts. Ohta et al. (2012) also tested the utility of real-time GPS in detecting coseismic displacements, linking them to tsunami forecasts. Chen et al. (2016) tested different rapid GPS-based source inversions for their utility in tsunami early warning for the 2014 Iquique earthquake, finding similarities in local tsunami amplitudes. The use of GNSS positions of cargo ships has been proposed as a useful data set for measuring tsunamis (Inazu et al., 2016). Chen et al. (2019) propose an automated joint local GNSS and regional seismic inversion for real time tsunami warning.

In this study, we take the first steps to systematically analyze the quality of near-field tsunami forecasts that would rely on earthquake

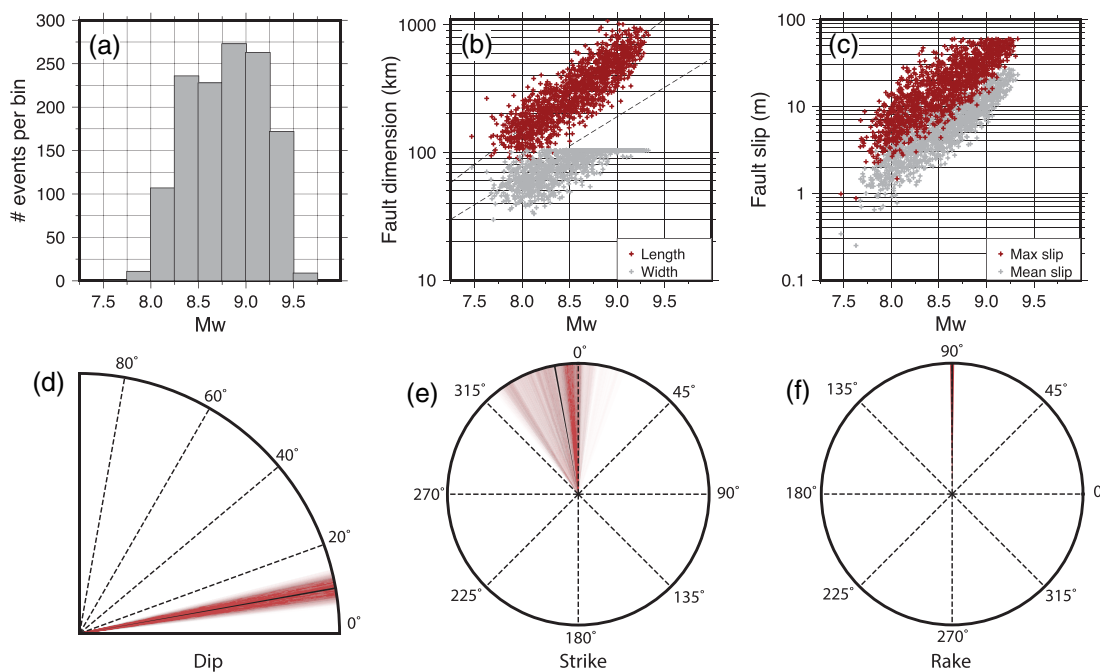


Figure 2. Summarized parameters for the synthetic rupture database from Melgar et al. (2016). (a) Distribution of earthquake magnitudes. (b) Fault length and width compared to magnitude-area scaling relations of Blaser et al. (2010). (c) Mean slip as a function of magnitude. (d) Range in mean fault dip per event. Mean of entire data set is marked with a solid black line. (e) Range in mean strike per event. (f) Range in mean rake per event.

We focus our study on potential local megathrust ruptures affecting the Cascadia subduction zone (CSZ; Figure 1). The CSZ, located off the Pacific Northwest of the United States and southwestern Canada, has a high potential to generate a large tsunamigenic earthquake in the future. The last large ($M > 8$) earthquake in this region was in 1700 (Satake et al., 1996). Tsunami models based on Japanese records of an “orphan tsunami” from the same time advocate that the earthquake likely occurred over the entire CSZ megathrust (Satake et al., 2003). Paleotsunami studies along the Pacific Northwest also corroborate with tsunami models and identify multiple possible large tsunamigenic earthquakes rupturing in the centuries prior to the 1700 event (Atwater et al., 1995; Nelson et al., 1995; Witter et al., 2011). Though estimates vary by study, the CSZ has a paleotsunami deposit derived recurrence interval of about 500 years (Peters et al., 2007). This indicates that the region has the potential for future large and damaging events. In addition to its expected tsunami hazard, the CSZ is an ideal environment as it also has a large number of deployed real-time GNSS sensors, allowing for the potential for a higher degree of resolution in source inversion studies (Figure 1). Currently, data streams from 213 stations are processed and broadcasted to end users including the National Oceanographic and Atmospheric Administration (NOAA) (Melgar et al., 2020). This is complemented by additional stations that are part of smaller networks such as the Bay Area Regional Deformation (BARD), the Pacific Northwest Geodetic Array (PANGA), and international networks such as the Network of the Americas (NOTA). Future work will aim to test for rupture scenarios not originating on the CSZ megathrust such as splay faulting, and eventually, we will apply our models to other regions outside of the U.S. Pacific Northwest; GNSS networks are sparser.

2. Methods and Data

Below, we explain the three key components of this study: the database of earthquake-tsunami pairs that we use as our observations, the rapid earthquake characterization model, and the metrics that we use to grade the performance of this model. We also discuss how the rupture environment and data is treated and the main parameters used in the tsunami propagation code.

2.1. Event Database

A large data set of local tsunamigenic earthquakes is needed in order to test the efficacy of GNSS-based tsunami forecasts. However, the CSZ does not have a catalog of recorded significant events to use. Therefore, we

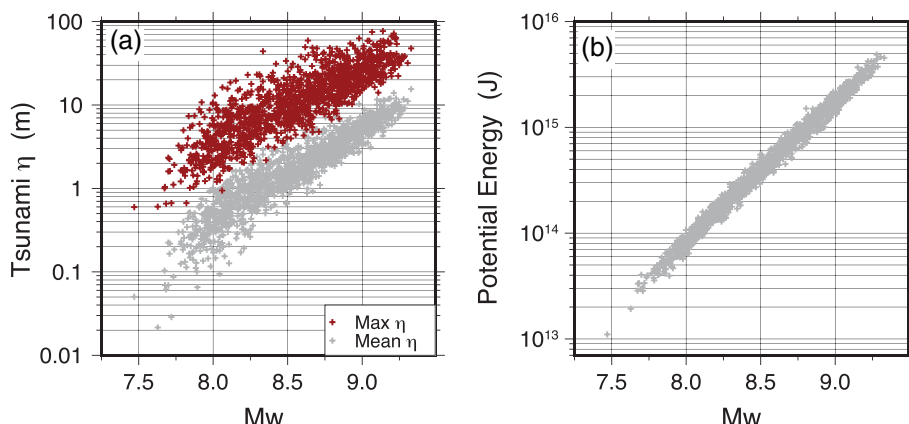


Figure 3. Summarized features of the tsunami generated from all 1,300 events. (a) Mean and maximum tsunami recorded along the coastline. (b) Tsunami potential energy for all 1,300 events.

use a database of 1,300 precomputed stochastic heterogenous slip scenarios from Melgar et al. (2016), which will act in this study as a set of synthetic observations. Key features of these ruptures, such as fault geometries, and slip are summarized in Figure 2. Features of the modeled tsunami for each of these ruptures are summarized in Figure 3. We use synthetic events, rather than a series of real global events for two important reasons. First, in order to test the limitations of rapid tsunami forecasting abilities, we need a dense data set of tsunami observations, primarily along the entirety of the local coastline. Accurately building such a data set requires exact knowledge of the earthquake source and the tsunami propagation. However, this exactness is nearly impossible to achieve with real events as every source model is the result of an inverse problem solution that has assumptions about the Earth's structure, noise, model resolution, and source smoothing. Second, even with perfect and dense observation data, we simply do not have enough large tsunamigenic earthquakes in modern history to use as our only source for model testing. For the purposes of reporting and testing a range of earthquake rupture scenarios, this study works better, at least initially, with synthetic data that can be modulated to test different model strengths and weaknesses. In future work, we will need models of many different types of faulting including splay faults, outer rise events, and strike-slip faults, over a range of station distances and with ranges of station noise, all for the same region. Then after a baseline for tsunami forecasting ability is set, real events with all their inherent uncertainties can be incorporated to further test modeling abilities.

Melgar et al. (2016) rupture database focuses on thrust events rupturing on the slab interface of the CSZ. This interface uses the slab geometry from McCrory et al. (2012) to a depth of 30 km. Rupture length and width are determined using magnitude dependent empirical scaling laws from Blaser et al. (2010) and then transposed onto our slab geometry. Slip is applied to the fault interface using the Karhunen-Loève expansion method described in Melgar et al. (2016) for Cascadia specific cases and more generally in LeVeque et al. (2016). This method assigns slip over each subfault using a von Karman correlation function, which has been found to replicate the statistics of slip distributions from past finite-fault solutions of moderate sized earthquakes (Mai & Beroza, 2002). The 1,300 events range in magnitude from Mw 7.5 to Mw 9.3; the range in slip and rupture geometry of these events are shown in Figure 2. The synthetic events tested in this study are treated equally and not assigned a magnitude-dependent likelihood through a Gutenberg-Richter distribution as is done in probabilistic tsunami hazard analysis. We are not attempting to forecast the likelihoods of future tsunamis, rather we focus instead on the ability to recreate key metrics of our source models, such as magnitude and tsunami impact. While this means that we are overemphasizing modeling at larger and less probably magnitude events, it also gives us an opportunity to assess our forecasting capabilities and identify any magnitude biases that we may occur at this extremum.

Using a Green's function approach linking motion at a GNSS station to slip on each subfault, we synthesize high rate (1 Hz) three-component GNSS waveforms for each rupture scenario. We follow the method of Zhu and Rivera (2002) to generate station-subfault impulse responses that are then convolved with the subfault's slip rate function (Melgar et al., 2016). This method uses an Earth structure model that is specific to Cascadia

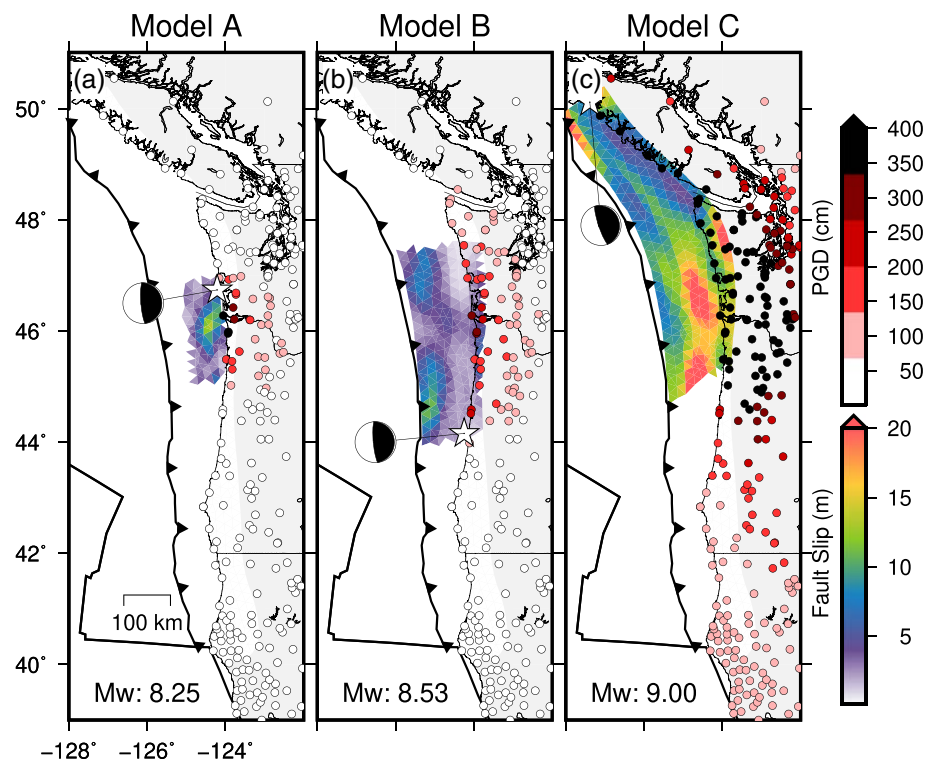


Figure 4. Rupture scenario and peak ground displacement for three scenario test cases. (a–c) Slip distribution for each scenario event overlaid on the larger, meshed, fault geometry. White star indicates the hypocentral location. Outlined colored circles mark the location of GNSS stations and are colored according to their observed PGD. Plate boundaries are approximate from Bird et al. (2003).

(Gregor et al., 2002). Waveforms are synthesized at the locations of 434 regionally located stations that could potentially be leveraged for use in early warning. Included stations are part of NOTA, PANGA, and BARD networks. Figure 1 shows the testing environment, including GNSS station locations, tectonic environment, and synthetic rupture extent.

In preparation for modeling the tsunami, we convert each rupture scenario to seafloor deformation by calculating the angular dislocations for triangular faults in an elastic half space (Comninou & Dundurs, 1975). This method is an adaptation from the Okada equations, which focus on rectangular faults (Okada, 1985). We assume an incompressible water column, allowing us to translate the seafloor deformation to a disturbance at the sea surface. This deformation initiates the tsunami, which is then modeled by solving the two-dimensional depth-averaged nonlinear shallow water equations using the openly available software package GeoClaw (Berger et al., 2011). GeoClaw previously underwent validation with the National Tsunami Hazard Mitigation Program using benchmark problems (Gonzalez et al., 2011). The edge of the model domain is treated as a nonreflective boundary. GeoClaw also allows the wet/dry boundary of the coastline to oscillate as the tsunami inundates along the coastline. Bottom friction is assumed to have a fixed Manning coefficient of 0.025 throughout the domain.

We use adaptive mesh refinement to optimize the computational cost of the tsunami model, which allows us to test a large database of scenarios. We model the tsunami in the open ocean with refinements that range from 4 arcmin to 15 arcsec. Because we are mainly interested in the tsunami along the coast of the United States, we use a define a narrow region immediately along the coastline where we fix the refinement to 3 arcsec for the entire duration of tsunami modeling. This finer coastal resolution allows us to better capture the maximum tsunami amplitude as the waves enter shallow water. We model each scenario for 2 hr of propagation time, which is enough to allow for the tsunami to propagate across the model domain. We log the tsunami maximum amplitude at the first wet pixel along the coastline with an observation point spacing of 90 m, yielding a dense database of the coastal tsunami response to complement our rupture database. In

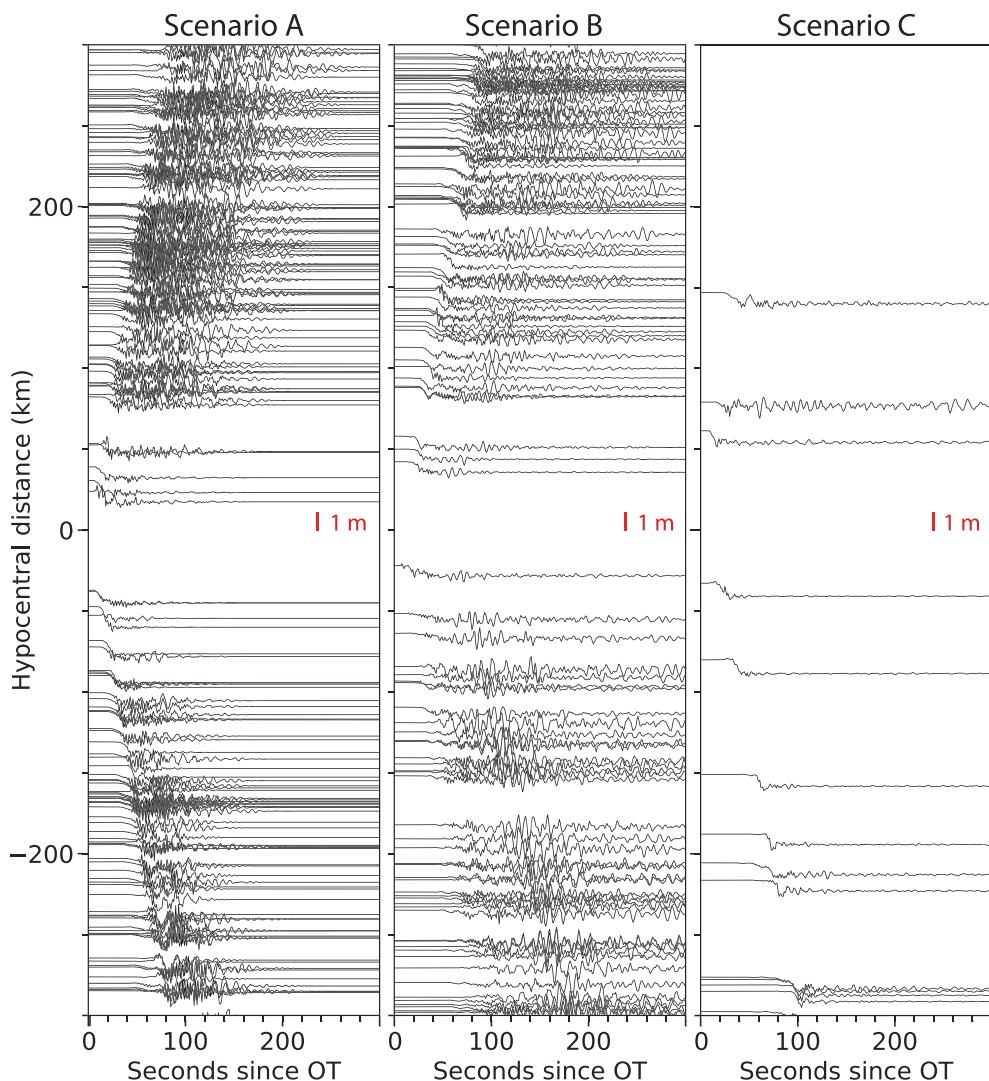


Figure 5. East-west component of all GNSS waveforms at hypocentral distances of 200 km or less for all three scenarios.

order to clearly present and compare the tsunami amplitudes along the coastline, we will present coastal amplitude results along a coarser 25 km along-coastline spacing.

The properties of the earthquake rupture database including peak slip and fault geometry and properties of the tsunami including mean and max coastal amplitudes are treated as our “known,” albeit synthetic, observations. We compare these properties with the output from the rapid earthquake module. Here we employ the GFAST earthquake early warning algorithm, which uses real-time, high-rate GNSS data located at local to regional distances. GFAST is divided into three modules which solve for the earthquake magnitude (Crowell et al., 2013; Melgar et al., 2015), a centroid moment tensor (Melgar et al., 2012), and a finite fault model (Crowell et al., 2012). GFAST has been used in simulated real time to analyze the sources of the 2010 Maule, 2014 Iquique, and 2015 Illapel, Chile earthquakes (Crowell et al., 2018) as well the 2016 Kaikoura, New Zealand earthquake (Crowell et al., 2018). This is the first time that GFAST is tested for its tsunami forecasting ability.

2.2. GFAST Modules

Here we summarize how GFAST operates in the context of this project; for further details, we refer readers to Crowell et al. (2012, 2013) and an operational flowchart in Crowell et al. (2016). As an earthquake occurs, GFAST initiates from a seismic trigger, currently from ShakeAlert (Kohler et al., 2020; Murray et al., 2018)

that provides the first estimate of the hypocentral location and origin time. This seismic trigger is necessary because GNSS data can have high ambient noise which could otherwise lead to false event triggering during quiescent periods (e.g., Kawamoto et al., 2016; Melgar et al., 2020). Since we are testing GFAST with synthetic events, we assume that the regional seismic network has triggered and located the event hypocenter. In regions with earthquake early warning systems such as ShakeAlert, this is trivial as the initial earthquake source characterization only uses a few seconds of P wave data for origin information. Once initiated, GFAST starts the three modules solving for magnitude, fault orientation, and distributed slip, respectively. The first module calculates magnitude by measuring the peak ground displacement (PGD). PGD is calculated from the three components of the GNSS waveform as follows:

$$PGD = \sqrt{N(t)^2 + E(t)^2 + U(t)^2} \quad (1)$$

The three-component GNSS waveforms, denoted as N , E , and U for north, east, and vertical components respectively in Equation 1, are all zeroed at the earthquake origin time, which removes any preevent drifts. Magnitude is derived from the PGD values of regional sensors using an improvement of the scaling laws proposed by Crowell et al. (2013) and Melgar et al. (2015),

$$\log_{10}(PGD) = A + B(M_w) + C(M_w)\log_{10}(R) \quad (2)$$

where A , B , and C , are the regression coefficients -6.687 , 1.5 , and -0.214 , respectively, M_w is the moment magnitude, and R is the distance between the earthquake source and station (Crowell et al., 2016). The expected uncertainty associated with PGD magnitude is ± 0.3 magnitude units (Crowell et al., 2016). We use this uncertainty as a metric for model performance. Ideally, a good model has an estimated magnitude inside these bounds.

The second module, running simultaneous to the PGD module, uses the static offsets from the same GNSS sensors to determine a geodetic centroid moment tensor (CMT) solution. The CMT module first conducts a grid search of the area surrounding the hypocenter to determine the best centroid location and then inverts for fault orientation. While the suite of synthetic ruptures follow the regional slab geometry and have a forced thrust component, the CMT inversion has no a priori constraints on centroid location, strike, dip, or rake. The best model solution is that which has the lowest residual to the GNSS offsets.

The third module constructs a coarse finite fault model from the nodal planes of the CMT solution. The dimensions of the planar fault are assumed from the scaling relations of Blaser et al. (2010) paired with the magnitude determined through the PGD module. While the length and width of the fault is allowed to vary, the number of subfaults is fixed and set to 20 along strike and 5 along dip. Finite fault models are constructed for both nodal planes of the moment tensor. The model with the larger variance reduction is retained as the best model and is used as the input for tsunami modeling. Since the subfaults in the GFAST module are rectangular, we use Okada (1985) for the seafloor deformation. This is ingested into the GeoClaw tsunami model using the same bathymetric model and output is collected at the same coastal locations as the suite of synthetic models.

2.3. Model Assessment Metrics

GFAST computes the magnitude, CMT, and time-independent finite-fault rupture of the earthquake, providing a solution every 30 s. At each output time, GNSS data that is circumscribed within a circular region centered at the hypocenter and whose radius is defined based on an assumed S wave velocity (here 3,000 m/s) is incorporated into the model. GNSS stations that are outside of this zone are assumed to have not yet experienced displacement related to the earthquake and are therefore excluded. We allow GFAST to continue to update the earthquake model until a final time of 300 s. GFAST is capable of providing information at shorter intervals (i.e., every second); however, this granularity is only necessary for earthquake early warning not tsunami warning. In our results, we show the GFAST model output at the 180 s epoch since origin time. While we could instead use the results from a later epoch, where most if not all GNSS data is available for every rupture, 180 s represents a temporal limitation of advanced warning.

In this study, we first focus on the results from three selected events out of the 1,300. We choose these because they are representative of the types of behavior we see in the larger data set. We then also show a synthesis of

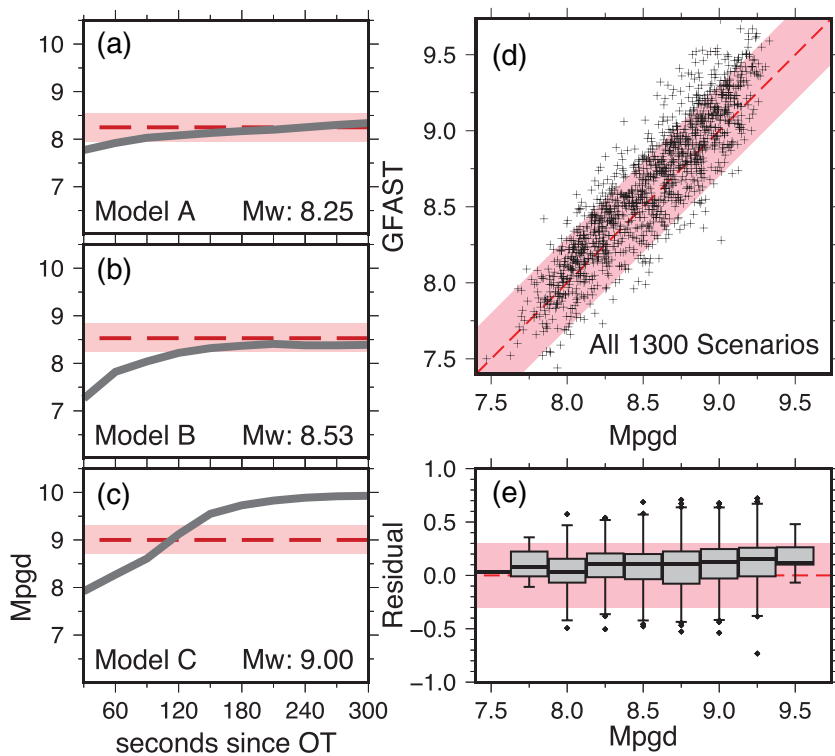


Figure 6. (a–c) Evolution of M_{PGD} with time for scenarios A–C. Light red shaded area indicates ± 0.3 magnitude units from the true magnitude. Red dashed line indicates to true magnitude. Target magnitude indicated in lower right corner. (d) Magnitude comparison between true magnitude and M_{PGD} at 180 s. E. Residual between GFAST and synthetic rupture scenarios. Scenarios are subdivided by the true event magnitude in 0.25 magnitude bins. Bounds of each box outline the first and third quartiles. The median is indicated by a thick black line and outliers are indicated by diamond shaped markers. The ± 0.3 magnitude units are indicated by light red shaded areas, and zero residual is indicated by a red dashed line.

GFAST performance for the database as a whole. The slip distribution for each of the three example ruptures is shown in Figure 4, and the east-west component of displacement local to the hypocenter for each of the three events is shown in Figure 5. Rupture onset time as a function of location on the fault plane for each scenario is available in Figure S1 in the supporting information. Model A has Mw 8.3 unilateral southward rupture with one asperity rupturing with a centralized peak slip of 12 m. Model B is a Mw 8.5 rupturing to the north with two discrete asperities, one near the hypocenter with a peak slip of 12 m, and another to the north with 8 m of slip. Model C is a Mw 9.0 rupture that initiates at the northwest edge of Vancouver Island propagating south with multiple complex regions of slip. The peak slip of 25 m occurs at the southern edge of the rupture, 230 s after origin time. Since all events occur on the slab interface, they all have predominantly thrust mechanism on a low angle ($\sim 9^\circ$) fault. These three events are highlighted to showcase both desirable and undesirable features of GFAST performance. While this study focuses on these three scenarios in detail, all results for all 1,300 scenarios are also available and published as a data set with this study (see Acknowledgments section).

We assess the performance of GFAST and the resultant tsunami forecast from the perspective of both how well the earthquake rupture is modeled and how well the tsunami amplitude at the coastline is forecast. For the PGD magnitude, we consider a good result to be an estimated magnitude that falls within 0.3 magnitude units of the true magnitude. The CMT and finite-fault results are assessed in tandem. A good GFAST result recreates the original strike, dip, rake, peak, and mean slip. We will show the fault plane geometry residual for the three scenario events as well as our general 1,300 databases.

Finally, we measure the tsunami forecast performance in two ways. First, we assess how well the tsunami amplitude along the coastline from the GFAST model approximate the corresponding tsunami from our database. In addition to testing the tsunami model fit across coastal transects, we use a sensitivity assessment method based on user defined thresholds that we believe is beneficial for local tsunami warning. In this

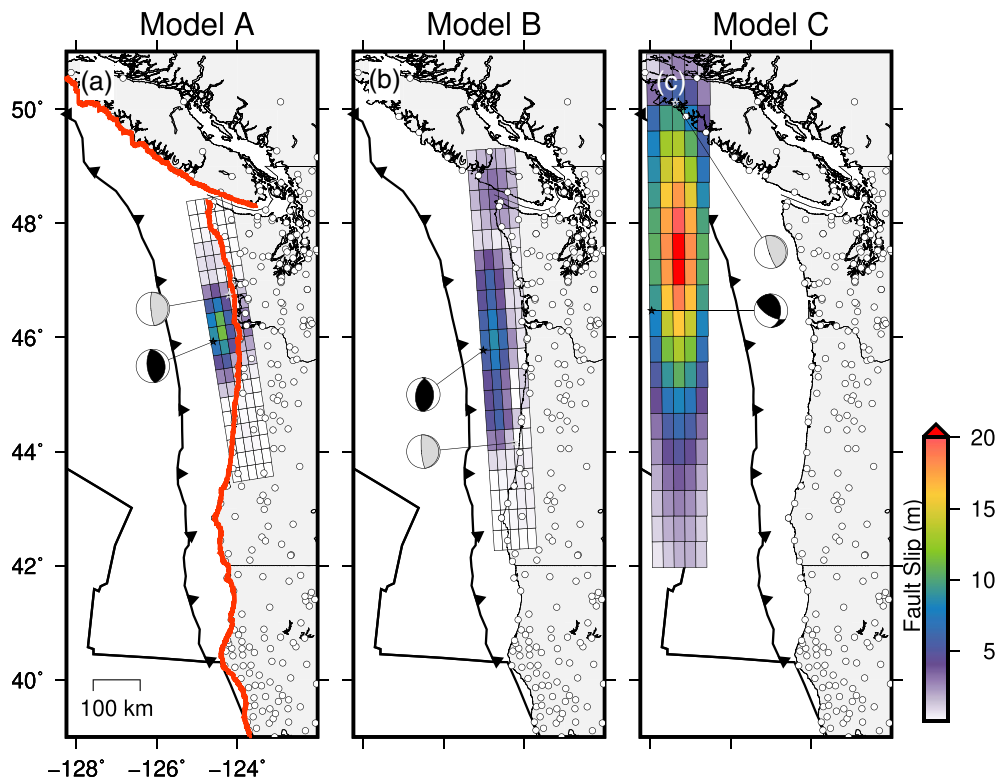


Figure 7. Resultant GFAST finite-fault solutions for scenarios A–C. Red transects A to A' and B to B' are the locations where the tsunami amplitude is calculated. Resultant tsunami along this transect is shown in Figure 8. White circles are the locations of GNSS sensors. The true slip values for each scenario are shown in Figure 4.

approach, a user defines a coastal amplitude threshold of interest, then the model is judged by its ability to correctly forecast where the tsunami did and did not exceed this coastal level. This loosely follows procedures to address the likelihood of exceeding set thresholds of ground motion in earthquake early warning (e.g., Minson et al., 2018). For a preset and user defined tsunami amplitude (e.g., 1 m), we can compute the percentage of instances for which both our scenario and rapid model forecast coastal amplitudes are in exceedance of this value. These instances would be considered as true positive forecasts. Similarly, we can compute the instances where both the scenario and model forecast that the tsunami will not exceed this value (true negative). The more locations that are identified as true positive and true negative, the higher the total model accuracy. Two ways that the model results can be erroneous are if the scenario tsunami exceeds the set benchmark at a location, but the model does not and the opposite: If the scenario tsunami does not exceed the benchmark, but the model does. These would be false positive and false negative forecasts, respectively. False negative forecasts are dangerous as coastal communities that should receive warnings and possibly evacuate are unwarned. False positives are also problematic because too many false positives erode confidence for future possibly correct forecasts (Yun & Hamada, 2015). By this metric, a good model would maximize the percentage of true positive and negative forecasts while minimizing false positive and negative forecasts. The philosophy here is that a specific user of a warning system sets the threshold at which an action is triggered. With this approach, by how much the tsunami exceeded the threshold is less important than simply correctly forecasting that the threshold was indeed exceeded. A similar analysis is used to look at forecasts of ground motion and intensity in the earthquake early warning field (Ruhl et al., 2019; Minson et al., 2019).

3. Results

3.1. PGD Magnitude

The first available output from GFAST is the earthquake's magnitude (M_{PGD}) using peak ground displacement. If the M_{PGD} for a given scenario is within the method uncertainty of 0.3 magnitude units, then we

Table 1
Fault Parameters for Scenarios A–C Compared With the Rapid Finite-Fault Solution

	Model Geometry			
	Strike	Dip	Rake	Peak slip (m)
Scenario A	355°	9.4°	90°	13.6
GFAST Estimate	351°	28.1°	74°	11.3
Scenario B	355°	9.5°	90°	11
GFAST Estimate	356°	38.6°	81°	8.67
Scenario C	341°	9.6°	90°	27
GFAST Estimate	359°	41.7°	109°	20.8
Mean Synthetic Database	349.6°	10.5°	90°	
Mean GFAST estimate	359.5°	40.1°	90.2°	

consider the result as successful. Figure 6 shows both the M_{PGD} estimates for the three scenarios at each epoch as well as the M_{PGD} estimate and residuals for all 1,300 ruptures at the 180 s epoch. Model A, which has a true magnitude of M_w 8.26, reaches a magnitude of 8.03 within 90 s and a magnitude of 8.17 by 180 s. Model B, which has a true magnitude of M_w 8.54, reaches a magnitude of 8.04 within 90 s and a magnitude of 8.37 by 180 s. Both models A and B satisfy our requirement to converge on an estimated magnitude that is within 0.3 units of the true magnitude. Model C, however, does not satisfy this requirement. While the rupture's true magnitude is 9.01, GFAST estimates a magnitude of 8.61 at 90 s and 9.73 by 180 s.

We assess all 1,300 scenarios at the 180 s epoch and M_{PGD} was correct (within ± 0.3 magnitude units) 82% of the time (1,069 of 1,300 scenarios).

For 18% of scenarios, M_{PGD} did not perform to our set standard. Figure 6 shows the comparison between true model magnitude and GFAST's M_{PGD} as well as the residual between true and estimated magnitude, divided into 0.25 magnitude unit bins. Among the large outliers (residuals exceeding ± 0.5), all save one case is due to an overestimate of M_{PGD} . The median residual for all 1,300 scenarios is +0.1 magnitude units meaning there is a slight tendency to overestimate the magnitude. Across all magnitudes bins tested, all scenarios that fall within the first and third quartiles of results fall within 0.3 units of true magnitude.

3.2. CMT and Finite Fault

Using the PGD informed magnitude to scale the fault length and width, an automated centroid moment tensor and finite-fault model is produced using the static offset provided from the regional GNSS network. The fault locations and slip distributions for the three scenario cases are shown in Figure 7. The differences in fault geometry between the synthetic ruptures and the GFAST rapid models are shown in Table 1. In all three cases, the focal mechanism was identified to be primarily thrust; however, the generated fault planes converge at a much steeper dip ($\sim 30^\circ$) than the actual sources which have a predominant dip of 9° . While the strike in all three cases recreates a roughly north-south rupture plane, there is a large discrepancy in Scenario C shown in Figure 7. In Scenario C, the true strike is 341° and the estimate is 359°. While this discrepancy is relatively small, due to the earlier overestimate of the fault magnitude which leads to a larger model fault length, it amounts to a large east-west offset between where slip occurs in the scenario and where slip is modeled. Larger full rupture cases like Scenario C also highlight GFAST's current limitation in using planar faults even when the environment requires a bend or change in strike to fully account for ruptures extending from Washington, USA, into Vancouver Island, Canada, or vice versa.

In complement to Figure 2, Figure 8 shows the comparison on mean slip, max slip, and fault geometry for all 1,300 scenarios. GFAST slightly underestimates both peak and mean slip compared to the finite faults available in the synthetic database. The mean residual between GFAST and the database models for mean and max slip is -2.6 and -1.4 m, respectively; however, these residuals are highly magnitude dependent (Figure S3).

GFAST's performance determining the fault geometry can be summarized by comparing the mean strike, dip, and rake of all the database events against the mean strike, dip, and rake of the preferred nodal plane derived by GFAST. These fault parameters are displayed in Figure 2 for the database cases, where the average strike, dip, and rake along with the standard deviations of each are: $349.6 \pm 11.1^\circ$, $10.5 \pm 1^\circ$, and 90° , respectively. The standard deviation of the rake for the database cases is zero because all earthquakes have forced pure thrust component. Figure 8 shows the average strike, dip, and rake along with the standard deviations of the ensemble of GFAST solutions as $359.5 \pm 50.6^\circ$, $40.1 \pm 10.3^\circ$, and $90.2 \pm 18.2^\circ$, respectively. Both the database and GFAST mean fault geometries are also recorded in Table 1.

When looking at results between the database events and GFAST, the dominant thrust component is reliably recovered across all events. In no scenario tested did GFAST estimate a strike-slip or normal faulting rupture. GFAST does not do a good job at determining the shallow depth of the megathrust interface. Instead, GFAST preferred fault planes reliably assign a much steeper $>30^\circ$ dip.

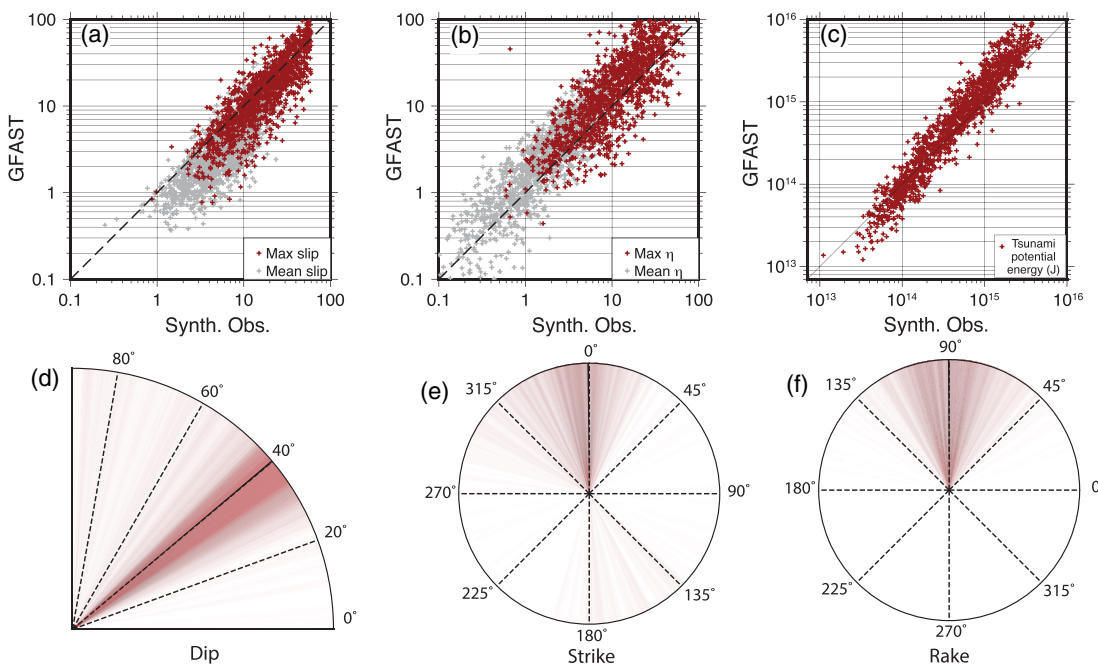


Figure 8. Summarized results between the synthetic database and GFAST. (a) Mean and maximum slip across each finite fault plane. (b) Mean and maximum amplitude tsunami along the coastline of the Pacific Northwest. (c) Tsunami potential energy, measured in Joules (J). (d) Range in mean fault dip per preferred GFAST nodal plane. Mean of entire data set is marked with a solid black line. (e) Range in mean strike per event. (f) Range in mean rake per event.

To assess the total seafloor deformation, which accounts for the relationship between depth, dip, and slip, we also calculate and compare the tsunami potential energy over the area A between each database and GFAST models as

$$PotE = \frac{1}{2} \rho g \iint \eta^2 dA \quad (3)$$

where the density of seawater is ρ , g is gravity, and η is the sea surface amplitude. Despite differences in fault geometry, both GFAST and the database models are in good agreement (Figure 8). While the tsunami potential energy is a known proxy for the near-field tsunami impact, (Nosov et al., 2014), it cannot fully replace analysis of the spatial extent and intensity of the tsunami along coastlines.

3.3. Coastal Tsunami Amplitudes

The tsunami for each finite fault model is computed, and the tsunami amplitude is shown along two transects in Figure 9: A to A' running from west to east along Vancouver Island and B to B' running from south to north along the U.S. west coast, as shown on the map in Figure 7. Scenario A's synthetic rupture produces a peak coastal amplitude of 5.6 m near 46°N. The GFAST solution for this same event produces a tsunami with a peak amplitude at the same location but is slightly larger, at 6.8 m. Similar to its bimodal slip distribution, scenario B has two zones of peak coastal amplitude, both above 6 m. The rapid fault solution did not distinguish between these two zones and instead has a smoother solution resulting in one central peak of 7 m. The finite fault solution for scenario C did a poor job recreating the original slip and this translated to a poor recreation of the expected tsunami. The rapid model results greatly overestimate the tsunami amplitude at northern latitudes (observed at 8 m but modeled in excess of 15 m).

We assess the tsunami forecast error at each coastal site by calculating the residual between the true and modeled amplitude at each binned location, where each bin is 25 km in length. A comparison between the mean and maximum recorded coastal tsunami between the database and GFAST for all 1,300 events (Figure 8) shows a total mean and max residual of +1.7 and +9.0 m, respectively, indicating an overestimate. The residual increases with increasing magnitude. The maximum residual related to smaller magnitude

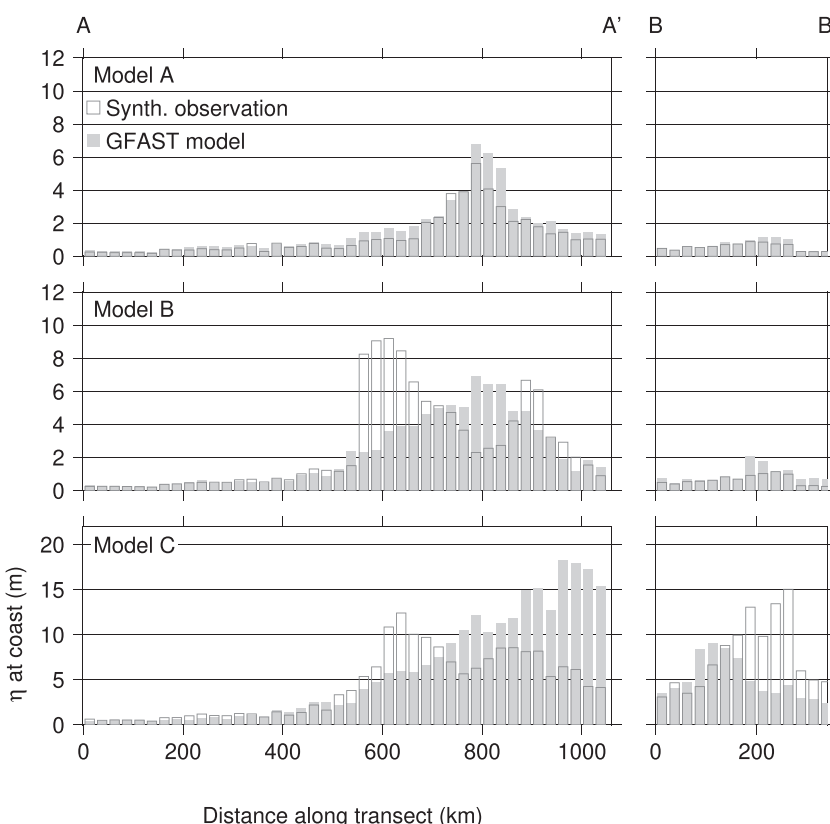


Figure 9. Bar graphs show the observed (hollow) and modeled (gray) tsunami along transect A to A', following the coastline of Vancouver Island and transect B to B' following the coastline of the U.S. West Coast. (Transect trace is outlined in red Figure 7.)

(and thus typically smaller tsunami events) events is -30 cm while events with a magnitude greater than 9.0 see residuals greater than 9 m (Figure S3).

A metric to compare the model and observed tsunamis is to plot the maximum tsunami for every location along the discretized coastline for every model run in a large scale and aptly named confusion matrix (Figure 10). Here model results for every scenario are categorized by how much they over or underestimate the database result down to a resolution of 25 cm. If every GFAST derived tsunami, plotted on the x axis, perfectly predicted the observed tsunami, and plotted on the y axis, at the exact same locations along the coast, then all values on the confusion matrix would be concentrated on the diagonals, similar to an identity matrix. Any spread from diagonal shows the misestimate between model and observed. The color of the box indicates the frequency of occurrence. With the cases tested in this study, there is a tendency for the GFAST model to overestimate the tsunami when compared to the database model. This causes a higher frequency of occurrence away from the diagonal in the positive x direction. However, the frequency of times where the GFAST tsunami model greatly overpredicts the database models is low. GFAST predicts within 1 m of the true amplitude 65% of the time and within 25 cm 22% of the time. GFAST forecasts a tsunami that is more than 3 m off from the true value 16% of the time and more than 5 m off 10% of the time.

In a similar way, we can use a model sensitivity method (Figure 11) for each tested scenario as a way to convert the results of the confusion matrix into forecasting outcomes. In the case of model A, a modest sized tsunami impacted the coastline local to the source. This impact was largely recreated using the rapid GFAST model. With a goal of forecasting the presence of a tsunami of at least 1 m along regional coastlines, the GFAST model succeeded over 80% of the time: 27% of the coastline correctly forecasted a tsunami of at least 1 m and another 60% of cases correctly forecast that the tsunami would not reach 1 m. A false alarm was issued for 13% of localities, and at one location, the tsunami did exceed 1 m but was not accurately forecasted. If the benchmark value is lowered, then the percent of locations that experience a true positive forecast

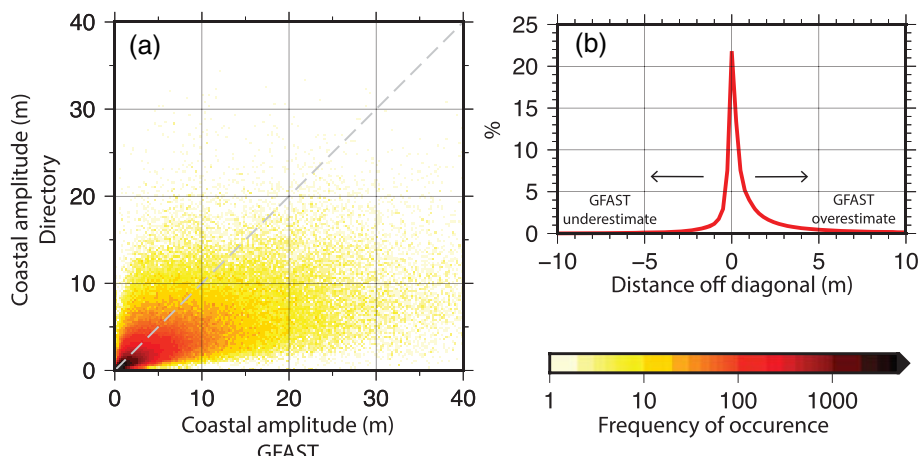


Figure 10. (a) Confusion matrix comparing maximum coastal amplitudes discretized at 20 km spacing along the coast for all 1,300 database events against the GFAST tsunami with the same coastal discretization. The color of each square indicates the density of occurrences in a log scale. (b) Percent occurrence of cases in reference to the diagonal.

increases, as most places will report some sort of tsunami impact. Conversely, as the threshold is raised to greater and greater values, the percentage of true negative forecasts increase. For larger magnitude cases, as shown through scenario C, the tsunami is large enough to affect the entire model space with coastal amplitudes of at least 30 cm. Therefore, even with a model result that grossly miscalculates details of the fault rupture, as is the case in scenario C, the modeled tsunami will still meet this minimum amplitude requirement, leading to a high percentage of true positive forecasts.

An average of the benchmark style forecasting abilities for all 1,300 scenarios is shown in Figure 12. Using a 30 cm tsunami amplitude threshold and our coastal discretization, we can correctly forecast the tsunami's arrival 90% of the time. This includes cases where we accurately forecast that there will be a tsunami as well as cases where we correctly forecast that there is not a tsunami. Table 2 shows the forecasting ability at 30 cm and 1, 3, and 5 m thresholds for each scenario, and Table 3 shows the averaged forecasting abilities for all scenarios. We pick these thresholds as guides as 30 cm to 1 m is a range where a U.S. tsunami advisory may be issued (Whitmore et al., 2008) where 3 to 5 m are also used as metrics in Japanese warning systems.

4. Discussion

Operational forecasting systems in the United States have traditionally relied on source models that use a linear combination of precomputed tsunami unit sources (Gica et al., 2008; Titov, 2009). Paired with observations from a sparse but global array of DART gauges, these unit sources allow for quick tsunami hazard assessments with a limited computational budget. However, the time that it takes for a tsunami to travel from the source to one of these gauges is often long enough that their use for near-field warning is limited (Williamson & Newman, 2018). In addition, a unit source approach cannot discern fault geometries that are not already in its database, leaving little room for the analysis of nontraditional or nonthrust events. Furthermore, correct earthquake magnitudes can be difficult to attain in the first few minutes following a rupture. As rupture scales increase with increasing magnitude, the variability in potential coastal tsunami intensities also grow (Melgar, Williamson, et al., 2019). In cases where larger earthquakes are expected, such as along Cascadia, the inclusion of nonuniform slipping rupture models, as shown here, has the potential to more accurately capture the variability in hazard along coastlines and to better identify peak slip.

With increasingly available high-performance computing, it is now possible to run a custom-built “on-the-fly” tsunami model within seconds to minutes, ending a reliance on precomputed sources (Angove et al., 2019). It also allows for more complex, heterogeneous slip rupture models. Faster computing shortens the period of time between acquiring and processing data and issuing alerts, making local and customizable alerts more feasible.

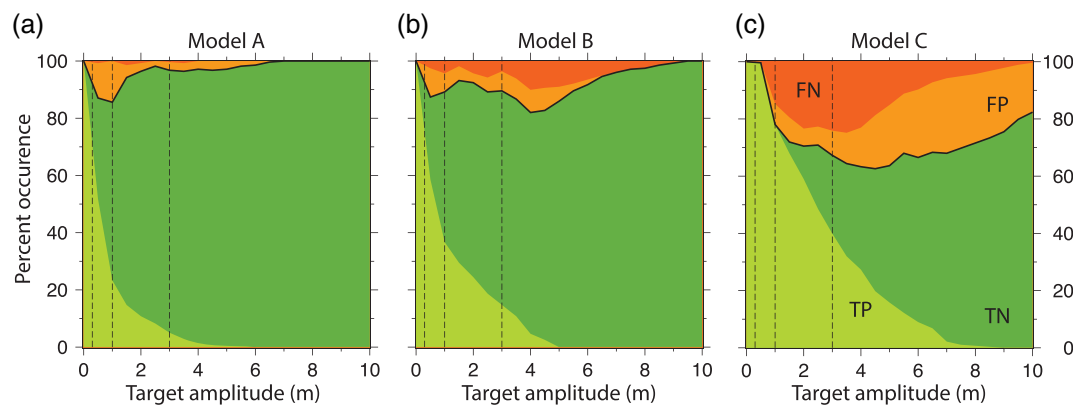


Figure 11. Tsunami forecasting capabilities at set benchmark amplitudes for the three scenario cases (a–c). Abbreviations TP, TN, FP, and FN indicate true positive, true negative, false positive, and false negative, respectively.

The first available information about the earthquake rupture from GFAST is a PGD informed magnitude. As shown in Figure 6, M_{PGD} does a good job approximating the true magnitude for most events with the first 180 s of available GNSS data; 82% of the scenarios tested converged toward the true magnitude. There are a few cases where our estimated magnitude has a residual outside of our self-imposed limits that define a “good” solution (± 0.3 magnitude units). A closer inspection of the ruptures associated with the M_{PGD} outliers shows that poorly performing scenarios always have at least one of the same two characteristics. The first is a purely unilateral rupture from a region with a low station density region to a region with high station density coupled with the majority of the moment release occurring proximal to this high-density area. An example of this is highlighted in this study’s scenario C (Figure 4c). Here the earthquake initiated offshore of northern Vancouver Island and ruptured south. The area within 300 km of the hypocenter has a station roughly every 50 km along the coastline and limited moment release. Further away the station distances decrease to roughly 10 km. This region also has the two main asperities that released the bulk of the seismic moment in the rupture. In these cases, the PGD magnitude component of GFAST overestimates the earthquake magnitude by up to 1 magnitude unit. The reason for this is that M_{PGD} assumes a point source, as a result, the large moment release far from the hypocenter is interpreted as originating from an extremely large magnitude event. With many more far-field stations registering large displacements and hence a larger magnitude than near-field stations with smaller levels of displacement, the M_{PGD} estimate skews toward fitting the high displacement far-field stations. This is a current limitation of the M_{PGD} approach which relies on the point source assumption being at least approximately true. Efforts are underway to overcome thus problem, for example, machine learning algorithms can be trained to identify magnitude based on GNSS waveforms, without the point source assumption and promise to be more robust in this (Lin et al., 2019).

The second case that causes large residuals is the reverse scenario: The majority of moment release occurring far from the hypocenter but in an area of low station density. This translates to an overwhelming number of stations reporting small amounts of ground displacement, which overshadows the few sparse stations that may experience the latent slip. Other unsuccessful M_{PGD} cases occurred largely offshore of Vancouver Island where the entire rupture is concentrated near the trench where the distances between source and station are greatest and with a limited near-field network. Examples of the ruptures where M_{PGD} typically fails are shown in greater detail in Figure S2. A goal for future versions of GFAST will incorporate better distance measures for M_{PGD} to account for the aforementioned issues.

A rapid and accurate magnitude determination is important when assessing the expected tsunami hazard, but it is an imperfect metric. Two earthquakes with the same magnitude can generate different sized tsunamis, particularly in the nearfield, depending on the details of the slip pattern, fault orientation, and centroid depth. The ability to accurately forecast coastal tsunami amplitudes minutes after earthquake rupture is ultimately the goal of local tsunami warning. In order to model the expected tsunami from source to the coastline, we first need the vertical component of seafloor deformation calculated using the GFAST finite fault outputs.

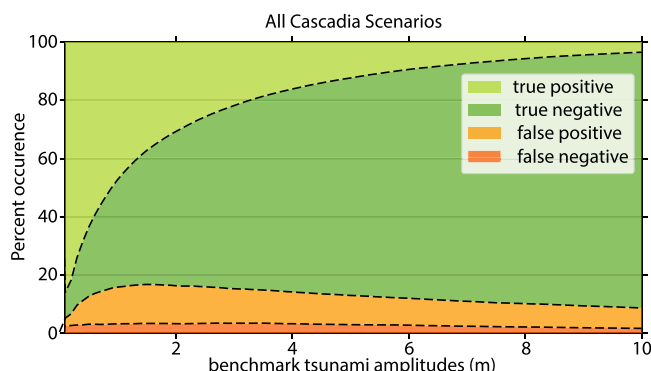


Figure 12. Averaged tsunami forecasting capabilities at set benchmark amplitudes ranging from 0 to 10 m for all 1,300 scenarios.

capture the spatial location of slip, an estimated focal mechanism, and total moment of the earthquake, which translates to useful information about the tsunami. A modeling approach that is conscientious of data uncertainties, fault geometries, and model regularization will always yield better results than a rapid approximation. However, in the case of tsunami early warning, these sorts of decisions often take time and are not feasible for local coastlines. For wholesale public acceptance and confidence, we must strive for more than “good enough” and the results shown here point to obvious necessary improvements to GFAST such as including a library of precomputed likely fault geometries such as the known location of the megathrust. In future versions of the code, the finite fault inversions on the two nodal planes from the CMT solution will compute against other candidate geometries. Ongoing research will show whether this solves the issue of outliers and tectonically unlikely geometries (i.e., Crowell et al., 2019).

Overall, earthquake characterizations through GFAST have demonstrated promise in rapidly capturing large megathrust events. The main utility of each rapid model is not how well each of the earthquake's characteristics are recovered, but what information can be reliably issued related to the expected tsunami intensity at the local coastline. While we show results for a range of coastal amplitudes (Figures 10 and 11), we focus primarily on our ability to accurately forecast a tsunami at 30 cm and 1, 3, and 5 m. The reason for these levels is that they represent tsunami intensities that require an actionable response through tsunami advisories and warnings. At 30 cm, an advisory may be issued and caution should be expressed when near affected coastlines. At 1 m, immediate surroundings around coastlines may be affected. At 3 m, the tsunami intensity is severe and at 5 m or greater; the tsunami is catastrophic (Whitmore et al., 2008). Even with imperfect knowledge on the exact distribution of slip or the exact earthquake magnitude, we are able to forecast if a tsunami will or will not affect the coast at these intensities with a high accuracy and few false alarms or missed alerts. For example: in Scenario C (Figure 11), even with an imperfect source geometry, the locations where the tsunami will have at least a 1 m tsunami, indicating action near the coast needs to be taken, or under 1 m, are correctly identified 90% of the time. The average accuracy across all scenarios tested is greater than 80% at the 1 m amplitude and slightly higher for most other tested amplitudes.

These assessments of tsunami impact can be made available within minutes of the earthquake rupture, along with information about the earthquake's location, focal mechanism, and magnitude, providing

The GFAST finite-fault ruptures can quickly identify thrust events from the provided GNSS data, modeling a coarse approximation of the earthquake rupture and providing more information on the tsunamigenic potential of an event than just the magnitude. However, finite-fault solutions are nonunique: Multiple different fault geometries and slip distributions may fit on-land GNSS data equally well. Without a priori constraints this can lead to fault models that are improbable for the given tectonic environment such as Scenario C and its error in identifying the best fault strike (Figure 7c).

At a first look, this can be problematic for real time tsunami modeling as the more accurate tsunami model will stem from a finite-fault source that closely resembles the original earthquake slip distribution. While these rapid models provide a limited description of the real slip distribution, they are nonetheless useful: They roughly cap-

Table 2

Breakdown of Forecasting Outcomes for Coastal Tsunamis of 30 cm and 1, 3, and 5 m for Each of the Three Scenario Cases

Threshold	Scenario A				Scenario B				Scenario C			
	30 cm	1 m	3 m	5 m	30 cm	1 m	3 m	5 m	30 cm	1 m	3 m	5 m
TP	83.3%	26.7%	8.3%	1.7%	85.0%	41.7%	16.7%	3.3%	96.7%	78.3%	58.3%	35.0%
TN	8.3%	60.0%	91.7%	96.7%	10.0%	51.7%	73.3%	78.3%	3.3%	15.0%	33.3%	46.7%
FP	8.3%	13.0%	0.0%	1.7%	5.0%	6.7%	3.3%	8.3%	0.0%	0.0%	5.0%	11.7%
FN	0.0%	0.0%	0.0%	0.0%	0.0%	0.0%	6.7%	10.0%	0.0%	6.7%	3.3%	6.7%
Accuracy	91.7%	86.7%	100.0%	98.3%	95.0%	93.3%	90.0%	81.7%	100.0%	93.3%	91.7%	81.7%

Note. TP, TN, FP, and FN are abbreviations for true positive, true negative, false positive, and false negative, respectively.

Table 3
Forecasting Outcomes at 30 cm and 1, 3, and 5 m, for the Averaged Data Set

Threshold	All 1,300 scenarios			
	30 cm	1 m	3 m	5 m
True Positive	74.0%	47.2%	21.8%	12.3%
True Negative	16.4%	37.0%	62.9%	74.7%
False Positive	6.8%	12.6%	11.8%	10.0%
False Negative	2.8%	3.2%	3.5%	2.9%
Total Accuracy	90.4%	84.2%	84.7%	87.0%
Total Error	9.6%	15.9%	15.3%	13.0%

GNSS noise (between 2 and 5 cm) is much lower than the expected signal (Melgar et al., 2020). In addition to traditional on-land GNSS, fully submarine data sets, such as pressure data from cabled networks, can provide key real-time and direct tsunami information for earthquakes (Gusman et al., 2014; Heidarzadeh et al., 2019; Howe et al., 2019; Kanazawa et al., 2016; Maeda et al., 2015). This data can then be incorporated into geodetic and seismic assessments, providing high-resolution models from trench to coastline, reducing some of the uncertainties common with geodetic models and highlighted above (Tsushima et al., 2014). As discussed in Angove et al. (2019), reducing uncertainty allows for a more effective public response as initial forecasts are issued with a higher degree of confidence. However, cabled arrays, which can potentially cover the entire rupture region of a subduction zone, are new, costly, and currently limited in spatial scope. Until proximal seafloor instrumentation is more ubiquitous, GNSS data, which is comparatively cheaper and is already deployed in most tectonically active regions, provides useful high-quality real-time data streams for regional events that can be leveraged for operational local tsunami warning.

5. Conclusion

In this study, we show results from testing a large synthetic data set against the GFAST rapid earthquake characterization module for megathrust ruptures along the CSZ. Even though there has not been a large tsunamigenic earthquake on the Cascadia megathrust in modern history, these tests help us to identify potential forecasting abilities as well as model and data limitations. These limitations and new directions, such as the inclusion of noise to GNSS waveforms, sparser GNSS networks, and the incorporation of nonthrust and nonmegathrust earthquakes, will be the focus of future research. Using displacement data available within the first 3 min following an earthquake, we can estimate an event magnitude within 0.3 units of the true magnitude for 80% of tested cases. This rapid earthquake magnitude is useful for a quick hazard assessment, but a forecast of the resultant tsunami at the coastline is valuable since tsunami hazards are dependent on a variety of other factors such as focal mechanism and the distribution of slip. When comparing our synthetic tsunami models to those created using the GFAST rapid source module, our performance is dependent on the goodness of the fault model, which can at times be erroneous due to limitations in data resolution with increasing distance offshore. However, tested scenarios are able to recreate the largely north-south striking dominantly thrust (and thus more tsunamigenic) rupturing earthquakes that are expected along the Cascadia margin. More work does, however, need to be conducted to constrain the fault dip, a parameter that may be better recovered if using a preprovided regional slab geometry. If we focus on our forecasting ability at predetermined coastal amplitude benchmarks, then we are able to create a timely forecast of the hazard at that benchmark value with an average accuracy greater than 80%. While this is far from perfect, it acts as a useful first approximation that is needed for near-field communities. As more direct data from offshore sources such as DART and tide gauges are acquired, more informed warnings can be issued for middle and far field communities.

Data Availability Statement

The stochastic slip models used in this study are publicly available from <https://zenodo.org/record/59943> website. The Clawpack/Geoclaw tsunami modeling code is openly available at <http://www.clawpack.org/> website. The model result and coastal tsunami amplitudes for every model in this study as well as simulated GNSS waveforms are publicly available from <https://zenodo.org/record/3677471> website.

actionable information for communities simultaneous to initial tsunami alert messages. Then, as more data is acquired from offshore pressure instruments and coastal tide gauges, the initial tsunami alert can be updated for middle to far field forecasts, using already tested and well-established methods for forecasting far-field hazard.

The use of GNSS for rapid source models fills the gap between tsunami initiation and the first direct observations of the tsunami tens of minutes later from open-ocean pressure gauges. Future work will test how the inclusion of noise will affect source models, particularly for smaller earthquake generated tsunamis. However, it is important to note that for larger events as are tested here, the typical range for

Acknowledgments

This work was funded in part by NASA grant 18-RRNES18-0001. D. A. was supported by the National Oceanic and Atmospheric Administration with this report being PMEL contribution 5066. Y. W.'s work is funded by the Joint Institute for the Study of the Atmosphere and Ocean (JISAO) under NOAA cooperative agreement NA15OAR4320063, contribution 2020-1067, and PMEL contribution 5066.

References

- Angove, M., Arcas, D., Bailey, R., Carrasco, P., Coetze, D., Fry, B., et al. (2019). Ocean observations required to minimize uncertainty in global tsunami forecasts, warnings, and emergency response. *Frontiers in Marine Science*, 6. <https://doi.org/10.3389/fmars.2019.00350>
- Aránguiz, R., González, G., Cienfuegos, R., Yagi, Y., Okuwaki, R., Urrea, L., et al. (2017). The 16 September 2015 Chile tsunami from the post-tsunami survey and numerical modeling perspectives. In *The Chile-2015 (Illapel) earthquake and tsunami* (pp. 219–234). Cham: Birkhäuser. https://doi.org/10.1007/978-3-319-57822-4_16
- Atwater, B. F., Nelson, A. R., Clague, J. J., Carver, G. A., Yamaguchi, D. K., Bobrowsky, P. T., et al. (1995). Summary of coastal geologic evidence for past great earthquakes at the Cascadia subduction zone. *Earthquake Spectra*, 11(1), 1–18. <https://doi.org/10.1193/1.1585800>
- Berger, M. J., George, D. L., LeVeque, R. J., & Mandli, K. T. (2011). The GeoClaw software for depth-averaged flows with adaptive refinement. *Advances in Water Resources*, 34(9), 1195–1206. <https://doi.org/10.1016/j.advwatres.2011.02.016>
- Bernard, E., & Titov, V. (2015). Evolution of tsunami warning systems and products. *Philosophical Transactions of the Royal Society A: Mathematical, Physical and Engineering Sciences*, 373(2053), 20140371.
- Bird, P. (2003). An updated digital model of plate boundaries. *Geochemistry, Geophysics, Geosystems*, 4(3), 1027. <https://doi.org/10.1029/2001GC000252>
- Blaser, L., Krüger, F., Ohrnberger, M., & Scherbaum, F. (2010). Scaling relations of earthquake source parameter estimates with special focus on subduction environment. *Bulletin of the Seismological Society of America*, 100(6), 2914–2926. <https://doi.org/10.1785/0120100111>
- Blewitt, G., Kreemer, C., Hammond, W. C., Plag, H. P., Stein, S., & Okal, E. (2006). Rapid determination of earthquake magnitude using GPS for tsunami warning systems. *Geophysical Research Letters*, 33. <https://doi.org/10.1029/2006GL026145>
- Bock, Y., Melgar, D., & Crowell, B. W. (2011). Real-time strong-motion broadband displacements from collocated GPS and accelerometers. *Bulletin of the Seismological Society of America*, 101(6), 2904–2925. <https://doi.org/10.1785/0120110007>
- Chen, K., Babeyko, A., Hoechner, A., & Ge, M. (2016). Comparing source inversion techniques for GPS-based local tsunami forecasting: A case study for the April 2014 M8.1 Iquique, Chile, earthquake. *Geophysical Research Letters*, 43, 3186–3192. <https://doi.org/10.1002/2016GL068042>
- Chen, K., Liu, Z., & Song, Y. T. (2019). Automated GNSS and teleseismic earthquake inversion (AutoQuake inversion) for tsunami early warning: Retrospective and real-time results. *Pure and Applied Geophysics*, 177(3), 1403–1423. <https://doi.org/10.1007/s00024-019-02252-x>
- Comninou, M., & Dundurs, J. (1975). The angular dislocation in a half space. *Journal of Elasticity*, 5(3–4), 203–216. <https://doi.org/10.1007/BF00126985>
- Crowell, B., Kwong, K. B., Williamson, A., Melgar, D., Arcas, D., Melbourne, T. I., & Scrivner, C. (2019). Testing different configurations of GNSS-based rapid source products for tsunami and ground motion characterization. In *AGU Fall Meeting 2019*. AGU.
- Crowell, B. W., Bock, Y., & Melgar, D. (2012). Real-time inversion of GPS data for finite fault modeling and rapid hazard assessment. *Geophysical Research Letters*, 39, L09305. <https://doi.org/10.1029/2012GL051318>
- Crowell, B. W., Melgar, D., Bock, Y., Haase, J. S., & Geng, J. (2013). Earthquake magnitude scaling using seismogeodetic data. *Geophysical Research Letters*, 40, 6089–6094. <https://doi.org/10.1002/2013GL058391>
- Crowell, B. W., Melgar, D., & Geng, J. (2018). Hypothetical real-time GNSS modeling of the 2016 Mw 7.8 Kaikoura earthquake: Perspectives from ground motion and tsunami inundation prediction. *Bulletin of the Seismological Society of America*, 108(3B), 1736–1745. <https://doi.org/10.1785/0120170247>
- Crowell, B. W., Schmidt, D. A., Bodin, P., Vidale, J. E., Baker, B., Barrientos, S., & Geng, J. (2018). G-FAST earthquake early warning potential for great earthquakes in Chile. *Seismological Research Letters*, 89(2A), 542–556. <https://doi.org/10.1785/0220170180>
- Crowell, B. W., Schmidt, D. A., Bodin, P., Vidale, J. E., Gomberg, J., Renate Hartog, J., et al. (2016). Demonstration of the Cascadia G-FAST geodetic earthquake early warning system for the Nisqually, Washington, earthquake. *Seismological Research Letters*, 87(4), 930–943. <https://doi.org/10.1785/0220150255>
- Fang, R., Shi, C., Song, W., Wang, G., & Liu, J. (2014). Determination of earthquake magnitude using GPS displacement waveforms from real-time precise point positioning. *Geophysical Journal International*, 196(1), 461–472. <https://doi.org/10.1093/gji/gjt378>
- Gica, E., Spillane, M., Titov, V. V., Chamberlin, C., & Newman, J. C. (2008). *Development of the forecast propagation database for NOAA's Short-Term Inundation Forecast for Tsunamis (SIFT)* (NOAA Tech. Memo. OAR PMEL-139). Seattle, WA: Pacific Marine Environmental Laboratory.
- Gonzalez, F., LeVeque, R. J., Varkovich, J., Chamberlain, P., Hirai, B., & George, D. L. (2011). GeoClaw results for the NTHMP tsunami benchmark problems. In *Results of the 2011 NTHMP Model Benchmarking Workshop*.
- Grapenthin, R., Johanson, I. A., & Allen, R. M. (2014). Operational real-time GPS-enhanced earthquake early warning. *Journal of Geophysical Research: Solid Earth*, 119, 7944–7965. <https://doi.org/10.1002/2014JB011400>
- Gregor, N. J., Silva, W. J., Wong, I. G., & Youngs, R. R. (2002). Ground-motion attenuation relationships for Cascadia subduction zone megathrust earthquakes based on a stochastic finite-fault model. *Bulletin of the Seismological Society of America*, 92(5), 1923–1932. <https://doi.org/10.1785/0120000260>
- Gusman, A. R., Murotani, S., Satake, K., Heidarzadeh, M., Gunawan, E., Watada, S., & Schurr, B. (2015). Fault slip distribution of the 2014 Iquique, Chile, earthquake estimated from ocean-wide tsunami waveforms and GPS data. *Geophysical Research Letters*, 42, 1053–1060. <https://doi.org/10.1002/2014GL062604>
- Gusman, A. R., Tanioka, Y., MacInnes, B. T., & Tsubshima, H. (2014). A methodology for near-field tsunami inundation forecasting: Application to the 2011 Tohoku tsunami. *Journal of Geophysical Research: Solid Earth*, 119, 8186–8206. <https://doi.org/10.1002/2014JB010958>
- Heidarzadeh, M., Wang, Y., Satake, K., & Mulia, I. E. (2019). Potential deployment of offshore bottom pressure gauges and adoption of data assimilation for tsunami warning system in the western Mediterranean Sea. *Geoscience Letters*, 6(1), 1–12.
- Howe, B. M., Arbic, B. K., Aucan, J., Barnes, C., Bayliff, N., Becker, N., et al. (2019). SMART cables for observing the global ocean: Science and implementation. *Frontiers in Marine Science*, 6, 424. <https://doi.org/10.3389/fmars.2019.00424>
- Inazu, D., Waseda, T., Hibiya, T., & Ohta, Y. (2016). Assessment of GNSS-based height data of multiple ships for measuring and forecasting great tsunamis. *Geoscience Letters*, 3(1), 25. <https://doi.org/10.1186/s40456-016-0059-y>
- Kanamori, H., & Rivera, L. (2008). Source inversion of W phase: Speeding up seismic tsunami warning. *Geophysical Journal International*, 175(1), 222–238. <https://doi.org/10.1111/j.1365-246X.2008.03887.x>
- Kanazawa, T., Uehira, K., Mochizuki, M., Shinbo, T., Fujimoto, H., Noguchi, S., et al. (2016). *S-net project, cabled observation network for earthquakes and tsunamis* (pp. 1–5). Dubai: SubOptic.

- Kawamoto, S., Hiyama, Y., Ohta, Y., & Nishimura, T. (2016). First result from the GEONET real-time analysis system (REGARD): The case of the 2016 Kumamoto earthquakes. *Earth, Planets and Space*, 68(1), 190.
- Kohler, M. D., Smith, D. E., Andrews, J., Chung, A. I., Hartog, R., Henson, I., et al. (2020). Earthquake early warning ShakeAlert 2.0: Public rollout. *Seismological Research Letters*, 91(3), 1763–1775. <https://doi.org/10.1785/0220190245>
- Lin, J. T., Melgar, D., Thomas, A., & Searcy, J. (2019). Harnessing rupture determinism for early warning with GNSS and recurrent neural networks. In *AGU Fall Meeting 2019*. AGU.
- LeVeque, R. J., Waagan, K., González, F. I., Rim, D., & Lin, G. (2016). Generating random earthquake events for probabilistic tsunami hazard assessment. In E. L. Geist, H. M. Fritz, A. B. Rabinovich & Y. Tanioka (Eds.), *Global tsunami science: Past and future, Volume I. Pageoph topical volumes*. Cham, Switzerland: Birkhäuser. https://doi.org/10.1007/978-3-319-55480-8_2
- Maeda, T., Obara, K., Shinohara, M., Kanazawa, T., & Uehira, K. (2015). Successive estimation of a tsunami wavefield without earthquake source data: A data assimilation approach toward real-time tsunami forecasting. *Geophysical Research Letters*, 42, 7923–7932. <https://doi.org/10.1002/2015GL065588>
- Mai, P. M., & Beroza, G. C. (2002). A spatial random field model to characterize complexity in earthquake slip. *Journal of Geophysical Research*, 107(B11). <https://doi.org/10.1029/2001JB000588>
- McCrory, P. A., Blair, J. L., Waldhauser, F., & Oppenheimer, D. H. (2012). Juan de Fuca slab geometry and its relation to Wadati-Benioff zone seismicity. *Journal of Geophysical Research*, 117, B09306. <https://doi.org/10.1029/2012JB009407>
- Melgar, D., Bock, Y., & Crowell, B. W. (2012). Real-time centroid moment tensor determination for large earthquakes from local and regional displacement records. *Geophysical Journal International*, 188(2), 703–718. <https://doi.org/10.1111/j.1365-246x.2011.05297.x>
- Melgar, D., Crowell, B. W., Geng, J., Allen, R. M., Bock, Y., Riquelme, S., et al. (2015). Earthquake magnitude calculation without saturation from the scaling of peak ground displacement. *Geophysical Research Letters*, 42, 5197–5205. <https://doi.org/10.1002/2015GL064278>
- Melgar, D., Crowell, B. W., Melbourne, T. I., Szeliga, W., Santillan, M., & Scrivner, C. (2020). Noise characteristics of operational real-time high-rate GNSS positions in a large aperture network. *Journal of Geophysical Research: Solid Earth*, 125, e2019JB019197. <https://doi.org/10.1029/2019JB019197>
- Melgar, D., LeVeque, R. J., Dreger, D. S., & Allen, R. M. (2016). Kinematic rupture scenarios and synthetic displacement data: An example application to the Cascadia subduction zone. *Journal of Geophysical Research: Solid Earth*, 121, 6658–6674. <https://doi.org/10.1002/2016JB013314>
- Melgar, D., Williamson, A. L., & Salazar-Monroy, E. F. (2019). Differences between heterogenous and homogenous slip in regional tsunami hazards modelling. *Geophysical Journal International*, 219(1), 553–562.
- Minson, S. E., Baltay, A. S., Cochran, E. S., Hanks, T. C., Page, M. T., McBride, S. K., et al. (2019). The limits of earthquake early warning accuracy and best alerting strategy. *Scientific Reports*, 9(1), 2478–2413. <https://doi.org/10.1038/s41598-019-39384-y>
- Minson, S. E., Meier, M. A., Baltay, A. S., Hanks, T. C., & Cochran, E. S. (2018). The limits of earthquake early warning: Timeliness of ground motion estimates. *Science advances*, 4(3).
- Minson, S. E., Murray, J. R., Langbein, J. O., & Gomberg, J. S. (2014). Real-time inversions for finite fault slip models and rupture geometry based on high-rate GPS data. *Journal of Geophysical Research: Solid Earth*, 119, 3201–3231. <https://doi.org/10.1002/2013JB016022>
- Muhari, A., Imamura, F., Supparsi, A., & Mas, E. (2012). Tsunami arrival time characteristics of the 2011 East Japan tsunami obtained from eyewitness accounts, evidence and numerical simulation. *Journal of Natural Disaster Science*, 34(1), 91–104. <https://doi.org/10.2328/jnds.34.91>
- Mungov, G., Ebé, M., & Bouchard, R. (2013). DART® tsunameter retrospective and real-time data: A reflection on 10 years of processing in support of tsunami research and operations. *Pure and Applied Geophysics*, 170(9–10), 1369–1384. <https://doi.org/10.1007/s00024-012-0477-5>
- Murray, J. R., Crowell, B. W., Grapenthin, R., Hodgkinson, K., Langbein, J. O., Melbourne, T., et al. (2018). Development of a geodetic component for the US West Coast earthquake early warning system. *Seismological Research Letters*, 89(6), 2322–2336. <https://doi.org/10.1785/0220180162>
- Nelson, A. R., Atwater, B. F., Bobrowsky, P. T., Bradley, L. A., Clague, J. J., Carver, G. A., et al. (1995). Radiocarbon evidence for extensive plate-boundary rupture about 300 years ago at the Cascadia subduction zone. *Nature*, 378(6555), 371–374. <https://doi.org/10.1038/378371a0>
- Nosov, M. A., Bolshakova, A. V., & Kolesov, S. V. (2014). Displaced water volume, potential energy of initial elevation, and tsunami intensity: Analysis of recent tsunami events. *Pure and Applied Geophysics*, 171(12), 3515–3525. <https://doi.org/10.1007/s00024-013-0730-6>
- Ohta, Y., Kobayashi, T., Tushimura, H., Miura, S., Hino, R., Takasu, T., et al. (2012). Quasi real-time fault model estimation for near-field tsunami forecasting based on RTK-GPS analysis: Application to the 2011 Tohoku-Oki earthquake (Mw 9.0). *Journal of Geophysical Research*, 117, B02311. <https://doi.org/10.1029/2011JB008750>
- Okada, Y. (1985). Surface deformation due to shear and tensile faults in a half-space. *Bulletin of the Seismological Society of America*, 75(4), 1135–1154.
- Percival, D. B., Denbo, D. W., Ebé, M. C., Gica, E., Mofield, H. O., Spillane, M. C., et al. (2011). Extraction of tsunami source coefficients via inversion of DART buoy data. *Natural Hazards*, 58(1), 567–590. <https://doi.org/10.1007/s11069-010-9688-1>
- Peters, R., Jaffe, B., & Gelfenbaum, G. (2007). Distribution and sedimentary characteristics of tsunami deposits along the Cascadia margin of western North America. *Sedimentary Geology*, 200(3–4), 372–386. <https://doi.org/10.1016/j.sedgeo.2007.01.015>
- Riquelme, S., Bravo, F., Melgar, D., Benavente, R., Geng, J., Barrientos, S., & Campos, J. (2016). W phase source inversion using high-rate regional GPS data for large earthquakes. *Geophysical Research Letters*, 43, 3178–3185. <https://doi.org/10.1002/2016GL068302>
- Ruhl, C. J., Melgar, D., Grapenthin, R., & Allen, R. M. (2017). The value of real-time GNSS to earthquake early warning. *Geophysical Research Letters*, 44, 8311–8319. <https://doi.org/10.1002/2017GL074502>
- Ruhl, C. J., Melgar, D., Chung, A. I., Grapenthin, R., & Allen, R. M. (2019). Quantifying the value of real-time geodetic constraints for earthquake early warning using a global seismic and geodetic data set. *Journal of Geophysical Research: Solid Earth*, 124, 3819–3837. <https://doi.org/10.1029/2018jb016935>
- Satake, K., & Heidarzadeh, M. (2017). A review of source models of the 2015 Illapel, Chile earthquake and insights from tsunami data. *Pure and Applied Geophysics*, 174(1), 1–9. <https://doi.org/10.1007/s00024-016-1450-5>
- Satake, K., Shimazaki, K., Tsuji, Y., & Ueda, K. (1996). Time and size of a giant earthquake in Cascadia inferred from Japanese tsunami records of January 1700. *Nature*, 379(6562), 246.
- Satake, K., Wang, K., & Atwater, B. F. (2003). Fault slip and seismic moment of the 1700 Cascadia earthquake inferred from Japanese tsunami descriptions. *Journal of Geophysical Research*, 108(B11), 2535. <https://doi.org/10.1029/2003JB002521>

- Sobolev, S. V., Babeyko, A. Y., Wang, R., Hoechner, A., Galas, R., Rothacher, M., et al. (2007). Tsunami early warning using GPS-shield arrays. *Journal of Geophysical Research*, 112, B08415. <https://doi.org/10.1029/2006JB004640>
- Tang, L., Titov, V. V., Moore, C., & Wei, Y. (2016). Real-time assessment of the 16 September 2015 Chile tsunami and implications for near-field forecast. *Pure and Applied Geophysics*, 173(2), 369–387. <https://doi.org/10.1007/s00024-015-1226-3>
- Titov, V. V. (2009). Tsunami forecasting. In E. N. Bernard & A. R. Robinson (Eds.), *The SEA, volume 15: Tsunamis* (371–400). Cambridge, MA: Harvard University Press.
- Tsuji, Y., Satake, K., Ishibe, T., Kusumoto, S., Harada, T., Nishiyama, A., et al. (2011). Field surveys of tsunami heights from the 2011 off the Pacific Coast of Tohoku, Japan earthquake. *Bulletin. Earthquake Research Institute, University of Tokyo*, 86, 29–279.
- Tsushima, H., Hino, R., Ohta, Y., Iimura, T., & Miura, S. (2014). tFISH/RAPiD: Rapid improvement of near-field tsunami forecasting based on offshore tsunami data by incorporating onshore GNSS data. *Geophysical Research Letters*, 41, 3390–3397. <https://doi.org/10.1002/2014GL059863>
- Vargas, G., Farías, M., Carretier, S., Tassara, A., Baize, S., & Melnick, D. (2011). Coastal uplift and tsunami effects associated to the 2010 Mw8.8 Maule earthquake in Central Chile. *Andean Geology*, 38(1), 219–238.
- Vigny, C., Simons, W. J. F., Abu, S., Bamphenyu, R., Satrapod, C., Choosakul, N., et al. (2005). Insight into the 2004 Sumatra-Andaman earthquake from GPS measurements in southeast Asia. *Nature*, 436(7048), 201–206. <https://doi.org/10.1038/nature03937>
- Vigny, C., Socquet, A., Peyrat, S., Ruegg, J. C., Métois, M., Madariaga, R., et al. (2011). The 2010 Mw 8.8 Maule megathrust earthquake of central Chile, monitored by GPS. *Science*, 332(6036), 1417–1421. <https://doi.org/10.1126/science.1204132>
- Whitmore, P., Benz, H., Bolton, M., Crawford, G., Dengler, L., Fryer, G., et al. (2008). NOAA/West Coast and Alaska tsunami warning center Pacific Ocean response criteria. *Science of Tsunami Hazards*.
- Williamson, A. L., & Newman, A. V. (2018). Limitations of the resolvability of finite-fault models using static land-based geodesy and open-ocean tsunami waveforms. *Journal of Geophysical Research: Solid Earth*, 123, 9033–9048. <https://doi.org/10.1029/2018JB016091>
- Witter, R. C., Zhang, Y., Wang, K., Priest, G. R., Goldfinger, C., Stineley, L. L., et al. (2011). Simulating tsunami inundation at Bandon, Coos County, Oregon, using hypothetical Cascadia and Alaska earthquake scenarios. *Oregon Department of Geology and Mineral Industries Special Paper*, 43, 57.
- Wright, T. J., Houlié, N., Hildyard, M., & Iwabuchi, T. (2012). Real-time, reliable magnitudes for large earthquakes from 1 Hz GPS precise point positioning: The 2011 Tohoku-Oki (Japan) earthquake. *Geophysical Research Letters*, 39, L12302. <https://doi.org/10.1029/2012GL051894>
- Yue, H., & Lay, T. (2011). Inversion of high-rate (1 sps) GPS data for rupture process of the 11 March 2011 Tohoku earthquake (Mw 9.1). *Geophysical Research Letters*, 38, L00G09. <https://doi.org/10.1029/2011GL048700>
- Yun, N. Y., & Hamada, M. (2015). Evacuation behavior and fatality rate during the 2011 Tohoku-Oki earthquake and tsunami. *Earthquake Spectra*, 31(3), 1237–1265. <https://doi.org/10.1193/082013EQS234M>
- Zhu, L., & Rivera, L. A. (2002). A note on the dynamic and static displacements from a point source in multilayered media. *Geophysical Journal International*, 148(3), 619–627. <https://doi.org/10.1046/j.1365-246X.2002.01610.x>